Design of a Contactless Force Actuator via Active Air-Bearing for Substrate Handling

He, S.; van Ostayen, R.A.J.; Hassan HosseinNia , S.

Important note
To cite this publication, please use the final published version (if applicable).
Please check the document version above.

Design of a Contactless Force Actuator via Active Air-Bearing for Substrate Handling

Sifeng He ⬤, Ron A. J. van Ostayen ⬤, and S. Hassan HosseinNia ⬤, *Senior Member, IEEE*

Abstract—**Contactless handling systems for substrates hold significant potential in enhancing chip manufacturing yields by allowing the use of thinner and larger substrates, eliminating the risks associated with physical contact. This article introduces a novel contactless force actuator, employing the active air-bearing working principle, designed with a compact structure to effectively actuate substrates. The actuator features a continuous deformable air-bearing surface composed of compliant-based actuation unit cells, ensuring ease of fabrication to meet tight air-bearing tolerances. A modular design with seven unit cells is designed and manufactured to validate the performance. The results confirm that the proposed contactless actuator can be used to levitate and actuate the substrate simultaneously, in which case the maximum actuation force in the x-axis is determined to be 90 mN and a 42.5-μm fly height in the z-axis is achieved.**

Index Terms—**Actuator design, air bearing, compliant surface, contactless handling, thin film.**

I. INTRODUCTION

WITH the development of high-end electronics industries, the feature size of integrated chips has been optimized and reduced constantly in order to achieve lighter and smaller configurations [1]. In semiconductor and solar panel manufacturing industries, microchips are fabricated on thin silicon substrates with multistep processes (including deposition, patterning and etching, optical inspection, and packaging), where the thickness of the substrates is targeted to be decreased to reduce the material cost of substrates, and increase their working efficiency [2], [3]. However, once the thickness of the substrates gets too small (<200 μm), the substrates are extremely fragile and can be easily scratched or contaminated during the manufacturing processes [4]. Moreover, to further improve the productivity of chip manufacturing, the substrate size needs to be designed as large as possible, resulting in silicon substrates that are thin and large [5], [6], [7].

Thin and large-area silicon substrates mean that more damage will occur due to mechanical contact and direct interactions with the mechanical parts during the manufacturing processes of chips, which can result in a drop in productivity. In order to achieve high-yield manufacturing of chips based on thin but large substrates, a lot of efforts have been taken by pioneering researchers, especially in designing contactless actuation systems. Compared to other actuation systems, such as motor-based screw drive and piezo actuation with direct interactions of objects [8], [9], [10], [11], [12], [13], [14], contactless actuation systems can levitate objects on the top (or keep the objects floating at a certain height) and then actuate them in a mechanical contact-free manner.

Among the various applications in industries, plenty of electromagnetic-based contactless actuation systems have been well established [15], [16], [17], [18], [19]. However, their main downside is that only ferromagnetic materials can be suspended, which greatly narrows the application in the positioning/transportation of substrates for precision electronics since they are mostly made from silicon. Fortunately, there are still many technologies (including electrostatic actuation and air-based methods) that could be adopted for a wider range of object materials, especially silicon substrates. Specifically, electrostatic actuation could be an alternative since a wider range of target materials can be manipulated. Even so, there are some drawbacks of electrostatic actuation including the very small forces that can be generated and the requirement for high voltages to produce actuation force [20], [21].

In addition to the before-mentioned systems, air-based systems are more commonly adopted, especially for thin substrates, due to their applicability to various materials. Nevertheless, most of them are able to perform levitation only instead of contactless actuation as well, and examples of these include traditional air bearings [22], Bernoulli airflow [23], and ultrasonic vibrations [24], [25], [26]. Notably, air jets are an exception to that, in that they also use the Bernoulli airflow principle but with some inclined jetting structures to create a traction force to drive the object in-plane. The main issue here is that the air flow of directional air jets is more dynamic (with an externally pressurized air supply) and with a thicker air film, where the nonlinear aerodynamic effects induced by turbulent air flow will influence and degrade the performance of the system [27]. As a result, the systems based on air jets have not reached submicron level handling accuracy yet because of the inherent aerodynamic effects, which hinder the application in precision handling of fragile substrates [28].
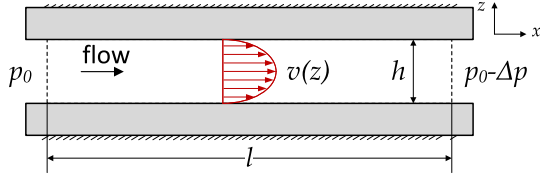
Fig. 1.　Poisseuille velocity profile of a fluid between two stationary plates due to a pressure drop Δp.
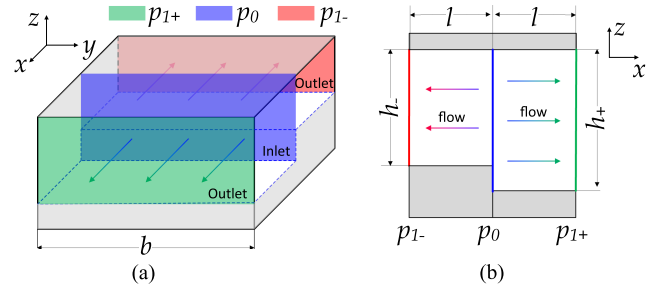

Fig. 2.　One degree of freedom actuation configuration with one inlet and two individual outlets. (a) 3-D configuration where the inlet pressure in the middle is higher than the outlet pressures at the boundaries. (b) Side view of the configuration.

To address the specific challenge at hand, this work proposes an innovative contactless force actuator employing an active air-bearing approach for substrate handling. Specifically, a novel continuous deformable air-bearing surface is designed using compliant design methods. In addition to this continuous deformable air-bearing surface concept, a compact modular system comprising seven unit cells is developed. The proposed contactless actuator prototype is analyzed, materialized, tested, and evaluated successfully, where the results prove that the proposed system can both levitate and actuate thin substrates.

In summary, the main contribution of this work is the design and development of a novel force actuator with a compact structural design combining good manufacturability and scalability, which can effectively actuate the substrate without any mechanical contact. The rest of this article is organized as follows. In Section II, the actuator design process is illustrated. In Section III, the developed modular design is validated and evaluated using FEA simulations. In Section IV, a series of performance tests are designed and performed experimentally. Finally, Section V concludes this article.

II. DESIGN OF THE CONTACTLESS FORCE ACTUATOR

In the first step, the mathematical analysis is provided using a 1-D analysis, which is intended to introduce the basic working principle of this design. Then a variable geometry air-bearing surface is introduced using a compliant, continuous surface, where the net traction force model is derived from the Reynolds equation. By implementing the idea of variable geometry and compliant unit cells, a new design with a continuous, deformable air-bearing surface is proposed.

A. Traction Force for Contactless Actuation

The flow of air in the thin lubricating film in an air bearing can be modeled using the Navier–Stokes equations for fluid flow. The air velocity profile between two stationary plates as a result of a pressure difference between inlet and outlet is depicted in Fig. 1. Introducing the standard thin film flow assumptions in the Navier–Stokes equations, the relationship between the velocity v and pressure p in this film in the x-direction can be expressed as

$$\eta \frac{\partial^2 v}{\partial z^2} = -\frac{\partial p}{\partial x} = -\frac{p_0 - (p_0 - \Delta p)}{l} = -\frac{\Delta p}{l} \quad (1)$$

where η is the dynamic viscosity of air. Here, it is assumed that there is a linear pressure drop between the entrance and the exit of the channel (Δp is much smaller than p_0), and therefore,

the pressure gradient is constant and equal to the given finite difference approximation.

Integrating twice with respect to z results, the velocity profile equation is derived as

$$v(z) = -\frac{1}{\eta} \frac{\Delta p}{l} \frac{z^2}{2} + c_1 z + c_2 \quad (2)$$

where c_1 and c_2 are the constants of integration. Applying the boundary conditions in terms of $v(0) = 0$ and $v(h) = 0$ these constants can be determined and the velocity profile equation can be rewritten as

$$v(z) = -\frac{\Delta p}{l} \frac{1}{2\eta} z^2 + \frac{\Delta p}{l} \frac{h}{2\eta} z. \quad (3)$$

At the plate interface, the flow has zero slip velocity and introduces a shear stress on the plate, which is used to obtain a contactless actuation force out of the flow.

This shear stress on the top plate is equal to the viscosity times the gradient of the velocity profile at the interface. Thus, the shear stress at the interface can be derived as follows:

$$\tau = -\eta \frac{\partial v}{\partial z}\bigg|_{z=h} = \frac{\Delta p}{l} \frac{h}{2} = -\frac{\partial p}{\partial x} \frac{h}{2}. \quad (4)$$

Based on the derived shear stress, the traction force density in the x-direction can be calculated as

$$\bar{F}_t = \frac{1}{l} \int_0^l \tau dx. \quad (5)$$

If the plates are rectangular with a width b, then we can get the traction force as

$$F_t = \iint \tau dA = \tau \cdot l \cdot b = \Delta p \frac{bh}{2}. \quad (6)$$

As shown in Fig. 2, the 1-DOF (degree-of-freedom) actuation configuration consists of one inlet and two outlets, where the net traction force can be expressed as follows:

$$F_t^{\text{net}} = (p_0 - p_{1+}) \frac{b \cdot h_+}{2} - (p_0 - p_{1-}) \frac{b \cdot h_-}{2} \quad (7)$$

where p_0 is the inlet pressure, p_{1+} and p_{1-} are the outlet pressures at the boundaries.

It can be seen that the pressure difference between the inlet and outlet, and the height are the key factors of the actuation performance.
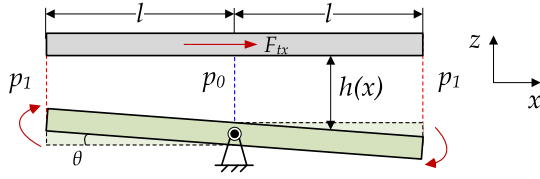
Fig. 3. Height variable geometry with tilting angle θ by actuating the rotational bottom plate.

Fig. 4. Pressure distribution profile of the inclined geometry, where l and b are set as 10 mm.

B. Variable Geometry for Air-Bearing Surface

Based on (7), the magnitude and direction of the net traction force can be controlled by either varying the outlet pressures p_1 or varying the geometry film height h. Between those, varying the geometry is more efficient dynamically and requires a less bulky system, since varying the pressure needs valves and air manifolds or chambers, which is not desirable for high bandwidth control and manufacturability when upscaling the system [29].

Therefore, a tilting mechanism is introduced into the height geometry (see Fig. 3), where the height can be described as

$$h(x, \theta) = h_0 + x \cdot \tan \theta \qquad (8)$$

where h_0 is the height at the tilting center ($x = 0$).

As the height is a function with respect to x, the pressure drop between p_0 and p_1 is not linear anymore, which means $\frac{\partial p}{\partial x}$ changes with the specific location. Hence, (6) and (7) are not valid anymore. Based on (4) and (5), a more general model of the traction force along the x-axis could be rewritten as

$$F_{tx} = \iint \tau_x dA = \iint -\frac{\partial p}{\partial x} \frac{h}{2} dA. \qquad (9)$$

In order to get the specific pressure distribution $p(x, \theta)$, the Navier–Stokes equations along the x-axis are simplified for the stationary thin film flow, which can be described by the Reynolds equation as

$$\frac{\partial}{\partial x} \left(-\frac{h^3}{12\eta} \frac{p}{R_g T} \frac{\partial p}{\partial x} \right) = 0 \qquad (10)$$

where R_g is the specific gas constant of air and T is the absolute temperature. Notably, since the pressure over the whole surface (from $x = -l$ to $x = l$) is not continuously differentiable because of the boundary condition at the center ($x = 0$), the following derivation of traction force is only for right half part (from $x = 0$ to $x = l$).

By integrating (10), the pressure p as a function of the x-coordinate and the tilting angle θ can be derived as

$$p^2(x, \theta) = \frac{p_0^2 - p_1^2}{h_0^{-2} - (h_0 + l \cdot \tan \theta)^{-2}} \cdot (h_0 + x \cdot \tan \theta)^{-2}$$

$$+ p_0^2 - \frac{p_0^2 - p_1^2}{1 - h_0^2(h_0 + l \cdot \tan \theta)^{-2}}. \qquad (11)$$
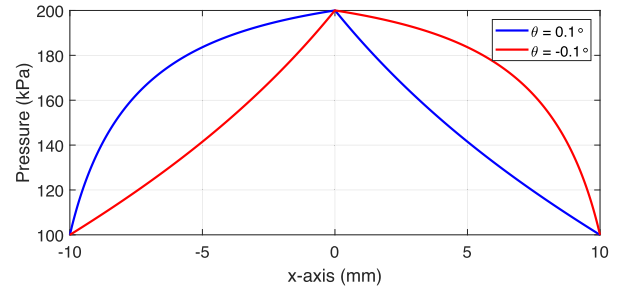
Based on (8), (9), and (11), the traction force in the x-axis with a certain tilting angle θ can be rewritten as

$$F_{tx}(\theta) = \iint -\frac{\partial (p(x, \theta))}{\partial x} \frac{h_0 + x \cdot \tan \theta}{2} dA \qquad (12)$$

$$F_{tx}(\theta) = \int_0^b \int_0^l -\frac{\partial (p(x, \theta))}{\partial x} \frac{h_0 + x \cdot \tan \theta}{2} dx dy. \qquad (13)$$

Regarding the whole geometry configuration, the net traction force can be calculated as

$$F_{tx}^{\text{net}}(\theta) = F_{tx}(\theta) - F_{tx}(-\theta). \qquad (14)$$

From these results, the pressure distribution of this height variable geometry with a certain tilt and the net traction force can be presented theoretically. As shown in Fig. 4, the pressure profiles show the asymmetry distribution from the center to each side. Specifically, the net force for a small tilting angle is obtained as: $F_{tx}^{\text{net}}(0.1°) = -F_{tx}^{\text{net}}(-0.1°) = 10.4$ mN. This shows that the variable height concept has the capability of outputting a 1-DOF force.

C. Continuous Deformable Air-Bearing Surface

A contactless handling system using this tilting surface concept has been proposed with a deformable air-bearing surface by Vuong [30], [31]. As implied by the name, this design has the capability of deforming or tilting the air-bearing surface to generate a viscous force to drive the substrates, instead of controlling the viscous forces by varying the pressures. However, the developed system has an issue concerning manufacturability. In particular, each actuator cell contains more than five individual mechanical parts, posing a big challenge for assemblage. Furthermore, the entire air-bearing surface is composed of many separate unit cells all separate from each other, which is a big challenge as well for surface flatness and roughness.

Given this challenge, a novel contactless handling system with a continuous deformable air-bearing surface is designed, which consists of compliant-based actuation unit cells (see Fig. 5). This whole mechanical structure contains two monolithic parts, in terms of the top part with a deformable surface and the middle part with air supply channels. It can be seen that the whole mechanical structure is compact and easy to assemble. Even the high-pressure and vacuum chambers are easy to integrate due to the simple two-layer configuration, thus there
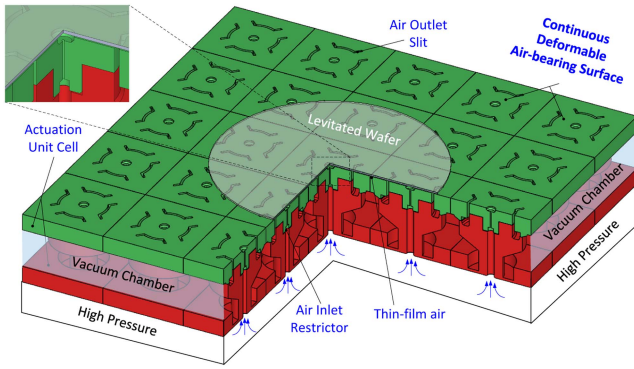
Fig. 5. Cross-sectional view of the designed contactless actuator for a handling system with compliant elements.
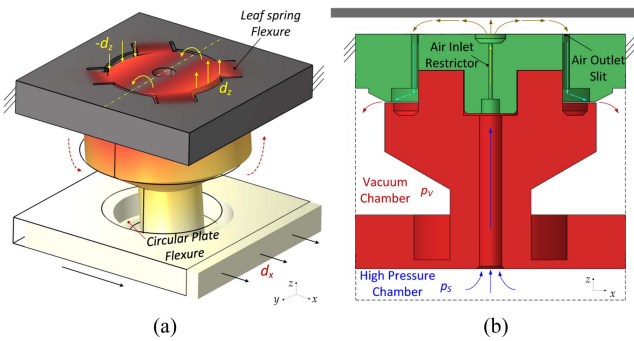

Fig. 6. Working principle of the single unit cell with the continuous deformable air-bearing surface. (a) Top surface is tilted due to the generated displacement in the x-axis (d_x). (b) Specific airflow path from the high-pressure chamber to the vacuum chamber.

Fig. 7. One degree-of-freedom modular design with seven unit cells for validation tests.

D. Modular Design With Seven Unit Cells

In the previous section, the contactless actuator with a continuous deformable air-bearing surface was introduced. In order to validate this design, a 1-DOF modular design with seven actuation cells has been designed. As shown in Fig. 7, the floating wafer is supported by seven hexagonal actuation unit cells (colored in green) to make optimal use of the available surface area, where the outside frame of cells is fixed with the base. Under the fixed top part, the bottom part is movable. Regarding the air supply, the vacuum chamber has two inlets (one for supply and one for sensing) and is sealed by flexible tapes, and the high-pressure supply is directly connected to each cell from underneath (see Fig. 5). In particular, the tilting of the surface can be implemented by exerting a force or displacement input on the movable bottom part. Moreover, it is worth mentioning that all unit cells are placed in different orientations, where each unit cell has an outlet slit placed close to the edge of the wafer. This kind of arrangement is made to make sure the outer unit cells have the same pressure boundary condition induced by the ambient air pressure from the edge of the wafer, which will be shown in the next section.

Specifically, the 2-D pressure distribution of the modular design with tilting deformation is more complicated than the 1-D model, due to the fact that the pressure distributions in the x- and y-direction are fully coupled. This pressure distribution in the lubricating film is described using the Reynolds equation, which is a second order partial differential equation that is derived from the Navier–Stokes equations using a list of the so-called "thin-film assumptions" [32]. Therefore, FEA analysis will be used in the next section to calculate the pressure distribution and the traction force.

is no need for complex manifolds anymore. Compared with the original deformable surface concept, in the new system, all deformable air-bearing surfaces of the actuation unit cells are integrated into one monolithic plate instead of many individual disconnected parts. This monolithic mechanical feature enables the whole system to be built with much less effort and cost, and also greatly increases the manufacturability level of the system.

As shown in Fig. 6, the deformable air-bearing surface of each actuation unit cell is a flexure-based structure. With respect to this design, the main frame is assumed as a rigid part and needs to be fixed with the ground reference, the central part with the inlet orifice and outlet slits is connected with the frame by adopting four leaf-spring flexures, which makes the part compliant. Notably, the central part is bonded with the middle part of the unit cell from underneath. Combined with the circular plate flexure on the bottom, the air-bearing surface will be tilted to some extent when a displacement is applied to the bottom in the x-axis (d_x) with respect to the top plate, where the net traction force due to the unevenly distributed air flow is along the opposite direction of d_x. By changing the direction and magnitude of the displacement in the xy plane, the air flow distribution under the wafer can be actively controlled to handle the wafer in a contactless way.
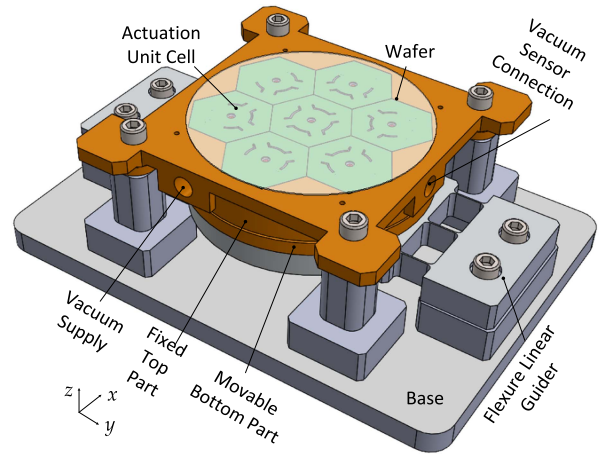
III. FEA VALIDATION AND EVALUATION

In this section, the unit cell is first optimized on the basis of the sweeping results of the simulation. Then, the elastic properties of the continuous deformable surface are modeled, resulting in a surface deformation profile. With the deformed
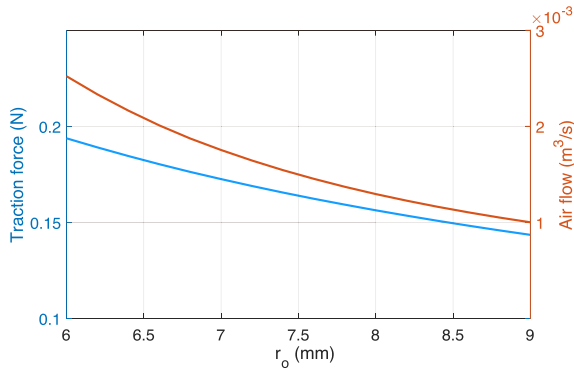
Fig. 8. Parametric sweeping results of r_o for traction forces and air flow consumption.

Fig. 9. Deformation profile of tilted actuation cells with 36.72 μm displacement input from the movable bottom part.

surface geometry, the pressure distribution and traction force are simulated.

A. Dimension Optimization for the Unit Cell

In order to maximize the traction force while maintaining the vacuum supply, the modular design with seven unit cells is optimized using the following steps. First, the total size of each unit cell is defined considering the size of the wafer and the number of cells. Second, the size of the circular recess part in the center of the cell is selected taking into account the relevant manufacturing limitations. Third, the radius of the vacuum outlet circular slits (r_o) is selected as the optimization key parameter.

Using COMSOL, a parametric sweep is carried out for r_o. As shown in Fig. 8, the results show that: with a constant fly height (30 μm), the air flow value decreases when r_o increases; with a constant tilt displacement, the traction force decreases when r_o increases. The results indicate that a higher traction force can be achieved with a smaller r_o, however, a smaller r_o will consume more vacuum supply. Clearly, there is a tradeoff between the traction force performance and the vacuum consumption. By taking the performance of the vacuum supply system into account (maximum pumping speed 0.0211 m³/s, Pfeiffer Hena 60), r_o is optimized to 8 mm with a vacuum consumption 0.0013 m³/s, which ensures the system has a high safety factor of 15 to maintain the vacuum supply pressure.

B. Validation of Continuous Deformable Surface

Since the continuous deformable surface is the key to the entire actuator design, the elastic deformation simulation is carried out first. As mentioned, the input is either force or displacement acting on the bottom surface along the 1-DOF direction (see Fig. 6), and in this simulation, we have selected to input a series of forces on the bottom part resulting in a series of displacement inputs. As shown in Fig. 9, the air-bearing surface with seven compliant unit cells is deformed evenly, where the tilted elements are in the same inclined direction. The result shows that the elements have a maximum 10.7 μm height increase and a maximum -10.7 μm height decrease with 36.72 μm displacement input, which proves that the capability of tilting is valid to change the height geometry. In addition, it is
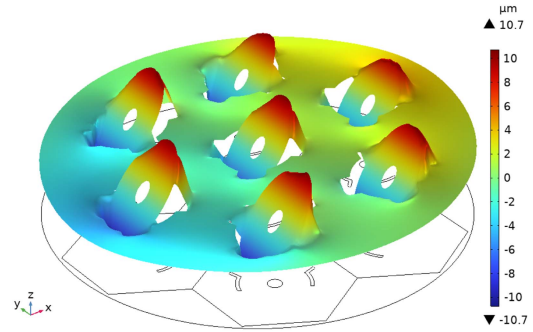
TABLE I
SIMULATION RESULTS OF TRACTION FORCE PERFORMANCE

Nr.	Displacement (μm)	Traction force (N)	Ratio (N/μm)
1	0.00	0.000000	-
2	7.34	0.006835	0.00093
3	14.69	0.013678	0.00093
4	22.03	0.020535	0.00093
5	29.38	0.027414	0.00093
6	36.72	0.034324	0.00093

worth mentioning that the outer ring of the vacuum slits closest to the ambient pressure of the seven cells have been partially sealed after some pretests, where a 0.1 mm-thin membrane is utilized to cover the slits close to ambient air to reduce the leakage of vacuum air. This is because of the weak performance of the experimental vacuum source.

C. Pressure Profile and Traction Force Validations

In order to validate the traction generated by the asymmetric thin film air flow, the numerical elastic deformation model has been extended with a thin film model based on Reynolds equation. For all models COMSOL Multiphysics has been used [33].

First, the vacuum pressure (air outlet pressure) is set to 80 kPa (absolute) based on the results from the pretests, and the ambient air pressure 100 kPa is defined as the boundary pressure at the wafer edges. Second, the high pressure for the air inlet is calculated to be equal to 195 kPa following the floating pressure equilibrium condition (If we assume that the weight of the substrate is negligible, the average pressure over the whole area must be equal to the ambient air pressure). With these specific settings, the pressure distribution profiles are simulated and obtained. Fig. 10 shows the pressure distribution difference between the condition without displacement input and the condition with displacement input, where the asymmetrical pressure distribution due to tilted geometry is clear and the contour shape matches with Fig. 4.

From this pressure distribution profile, the traction force can be integrated over the whole area by using (9). As shown in Table I, the traction forces with different displacement inputs are collected, which shows that 34.4 mN actuation force is achieved with 36.72 μm input. Moreover, the ratio between displacement
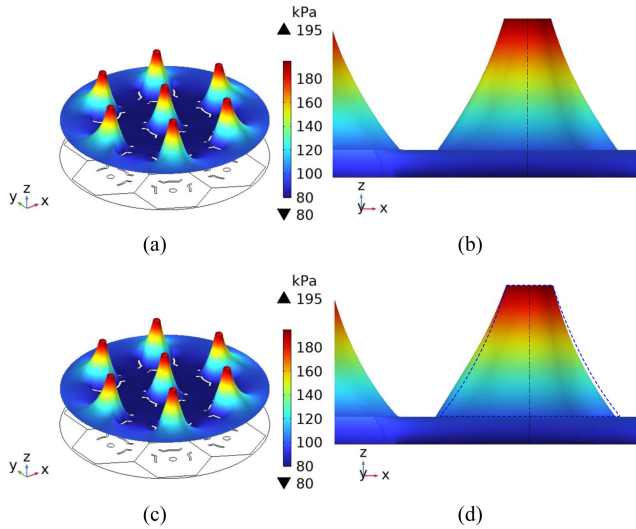
Fig. 10. Pressure distribution profiles. (a) Overview of the pressure without input. (b) Zoomed-in view of the pressure without input. (c) Overview of the pressure with 36.72 μm displacement input in the x-axis. (d) Zoomed-in view of the pressure with 36.72 μm displacement input in the x-axis.
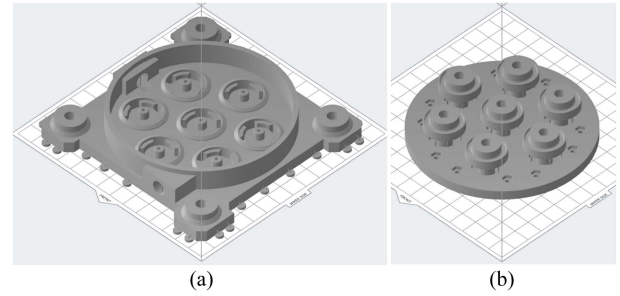

Fig. 11. 3-D printing settings for manufacturing monolithic parts in terms of the designed compliant top part and bottom part. (a) Top part adopting up-side-down printing orientation. (b) Bottom part.
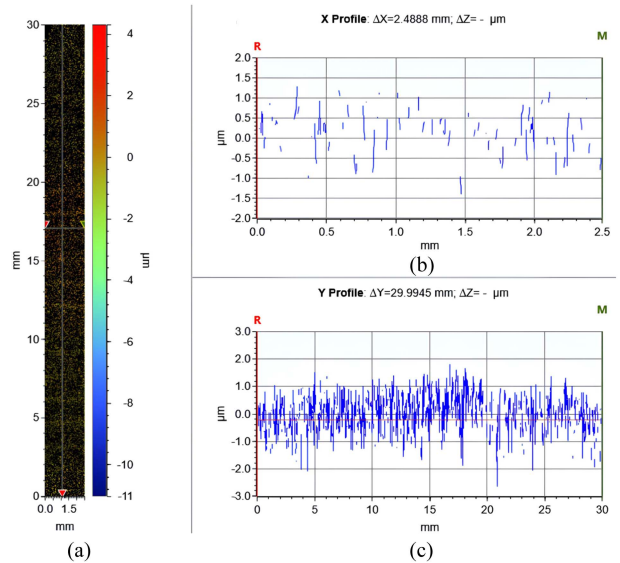

Fig. 12. Measurement results of the sanded surface quality. (a) Overview of the scanning area. (b) Scanning profile in the x-axis. (c) Scanning profile in the y-axis.

input and force output is constant, showing a linear relationship between displacement and force.

IV. EXPERIMENTAL TESTS AND RESULTS

In this section, the manufacturing processes are listed first. Then, the performance tests of the proposed design are implemented, including the manufacturing processes, flatness and roughness tests of the air-bearing surface, the fly height test, and the actuation force capability tests.

A. Manufacturing Processes and Tolerance Tests

The manufacturing of air bearing systems is challenging since air-bearing systems and in particular their surfaces are known for their tight manufacturing tolerances. First of all, stereolithography (SLA) 3-D printing is selected as the manufacturing method to fabricate the two main components, the top part containing the surface cells, and the middle part connecting the surface cells to the supply pressure and the vacuum outlet.

As shown in Fig. 11, the top part and the bottom part can be printed in one printing step, where a FormLabs 3+ printer is adopted and the Grey Resin is chosen due to its excellent performance for capturing small details. Specifically, the top part is placed upside-down to have a relatively flat and smooth surface for the active air-bearing. Even so, some warping or bending still happens on the main body after getting the parts off the building platform because of the residual heat stress during printing [34]. As a result, the top surface needs to be sanded in a postprocessing step to make sure that the top surface is flat and smooth enough to have a desirable air bearing. As shown in Fig. 12, the flatness and roughness of the sanded top surface are determined using a white light interferometer (Contour GT-K1, Bruker). The results show that the flatness fluctuation is less than

± 2 μm along a 30 mm length in the y-axis and the roughness is better than ± 1 μm, which is sufficient for the surface quality and further implementation of the air bearing.

Then, the printed and postprocessed two parts are glued together using Epoxy glue in between the unit cell interfaces, and a flexure linear guide for the movable bottom part is manufactured by CNC machining with 7075 aluminum alloy, which is then mounted on the bottom part. In summary, thanks to the compact structure design, the main components are fabricated and assembled in a cost-effective manner since no ultraprecise and laborious manufacturing techniques are involved to obtain tight tolerances.

B. Established Prototype Setup

As shown in Fig. 13, the prototype setup has been built up, where the PC host system and the data acquisition system (NI USB-6008, National Instrument) are not shown. In the prototype system, a micrometer (SM 50, Newport) is used to apply a displacement input for the movable bottom part along the x-axis,
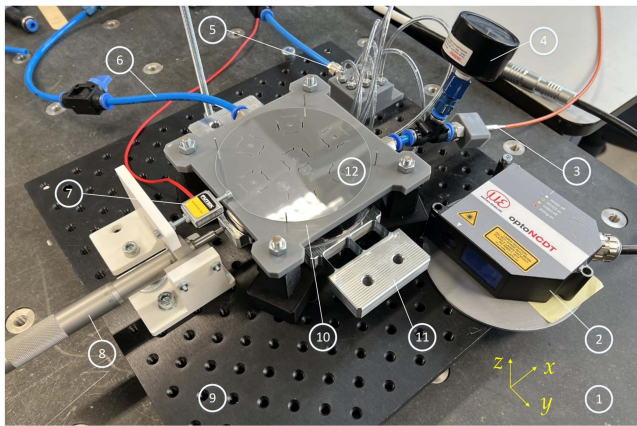
Fig. 13. Established prototype setup excluding PC host system and data acquisition system. (1) Granite base, (2) laser displacement sensor, (3) pressure sensor, (4) pressure gauge, (5) high-pressure air supply with a manifold, (6) vacuum air supply, (7) load cell, (8) micrometer, (9) breadboard, (10) sanded top part with unit cells, (11) flexure linear guide, and (12) 0.5 mm-thick 100 mm-diameter quartz wafer.
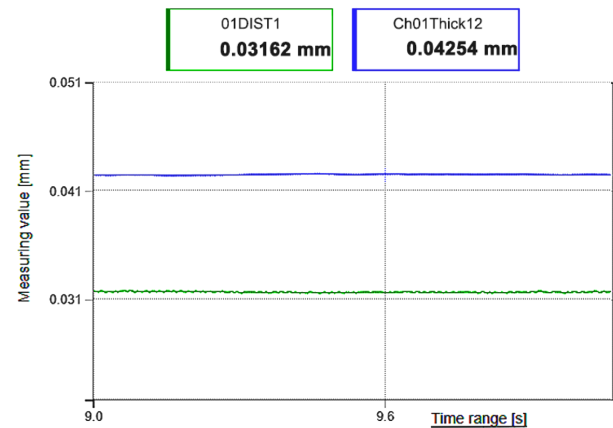

Fig. 14. Measurement result of the air film thickness using a confocal sensor, where the green line is the distance from the top boundary of the air film to the sensor, and the blue line is the thickness of the air film.
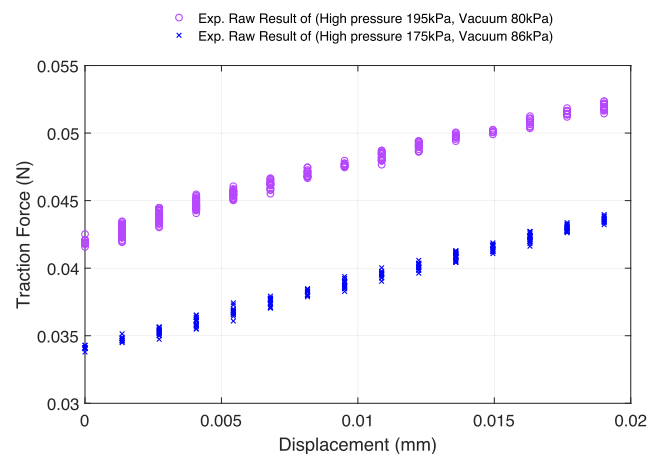

Fig. 15. Traction force performance with specific inputs.

where a laser displacement sensor (optoNCDT 2300, Micro-Epsilon) is placed on the side to measure the actual input. As a result of the displacement input, the cells on the top surface are tilted, where the air flow and pressure distribution are changed to have an actuation force on the wafer in the opposite direction of the input displacement. Then, the force is measured and recorded by the load cell (LSB200, FUTEK).

Apart from the mechanical parts, the high-pressure supply for seven unit cells is controlled by a pressure regulator and a 3-D-printed manifold is used to split the pressure source into seven equal inlets for the seven cells. Additionally, the vacuum supply is controlled by a vacuum pressure regulator and an extra vacuum gauge is connected to the vacuum chamber directly to detect the vacuum pressure. After some pretests, a digital pressure sensor (PAA-M5HB, KELLER) is added to the side of the vacuum gauge because of the pressure drift of the gauge.

C. Performance Tests

1) *Fly Height Test:* According to the simulation and pretest results, the vacuum pressure is set to 80 kPa (the deepest the system can get from the standard lab supply available), and the high pressure before the unit cell inlet restrictors is regulated to be equal to 380 kPa to get a stable 195 kPa on the air-bearing surface. Depending on the air supply, a laminar air-bearing thin film is formed, which allows the wafer to float above the system. Then, a test has been designed and performed to check the thickness of the air film (the fly height). Regarding the test setup, a confocal sensor (confocalDT IFS2407-0.1, Micro-Epsilon) is applied and mounted on the top of the wafer to measure the wafer height position. As shown in Fig. 14, the system is running stably with both vacuum and high-pressure supply on. The result shows that the thickness of the air film is 42.5 μm, which means the fly height is 42.5 μm.

2) *Actuation Force Capability Tests:* Now the levitation of the wafer has been confirmed, some tests for validating the actuation performance from the traction force are developed and implemented. First, a series of displacement inputs are applied on the bottom part, where the traction force outputs and actual displacement inputs are recorded simultaneously. As shown in Fig. 15, two sets of results with different vacuum and high-pressure supplies are obtained. It can be seen that the maximum traction force is 52 mN with 19 μm input and 80 kPa vacuum supply, and the maximum traction force is 44 mN with 19 μm input and 86 kPa vacuum supply; there are some inherent force offset from the beginning (43 mN for 80 kPa vacuum, 34 mN for 86 kPa vacuum).

Regarding these results, it is not clear if the large actuation force offsets are inherent to the system itself or the result of some other effect such as a deviation due to gravity. Therefore, another test is designed to examine this. As shown in Fig. 16, the recorded traction force has a high offset from zero with both vacuum and high-pressure supplies on (and there is no displacement input), and the traction force drops down to 3 mN when the vacuum is OFF, and thus, this huge decrease shows that the force offset is generated from the actuator system itself due
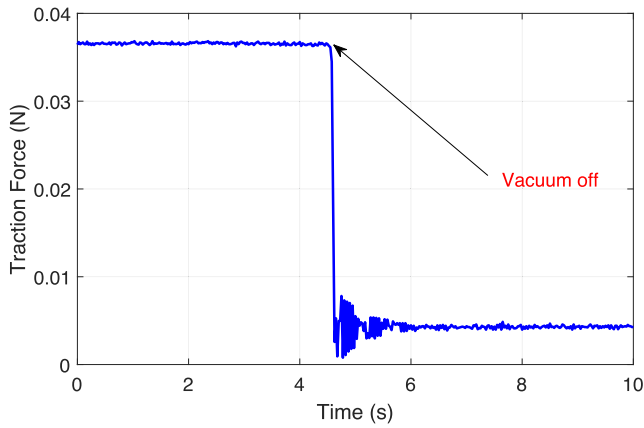
Fig. 16.   Inherent offset of traction force without input.

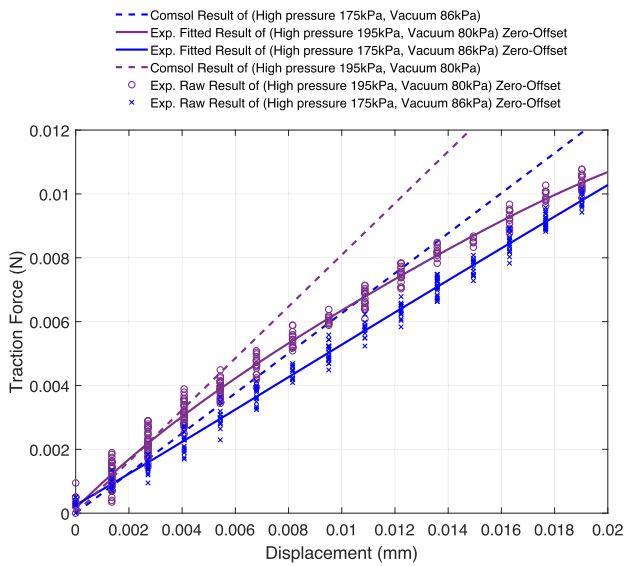Fig. 18.   Test results of the generated traction force based on the optimized vacuum supply.

Fig. 17.   Performance comparison between experimental results and simulation results (dash lines).

to some manufacturing or assemblage errors, especially for the inlets and outlets.

Assuming a constant offset, the data are shifted to zero, and compared to the modeled results (see Fig. 17). According to the results, it can be concluded that: the input-to-output ratios for both a 86 kPa and a 80 kPa vacuum pressure are nonlinear and keep decreasing when input increases, indicating some nonlinear effects; the experimental results do match with the simulation results for low values of the displacement; the result of vacuum 86 kPa is less nonlinear than the one of deeper vacuum condition in terms of 80 kPa, which means the vacuum performance is one of the factors for the nonlinearity.

3) Actuation Force Test With Optimized Vacuum Supply: Furthermore, using a deeper vacuum source the substrate is forced to come into contact with the compliant surface, and the location of the initial point of contact is used to study the (non)uniformity of the vacuum pressure in the chamber. Specifically, if the location of the contact point is not in the
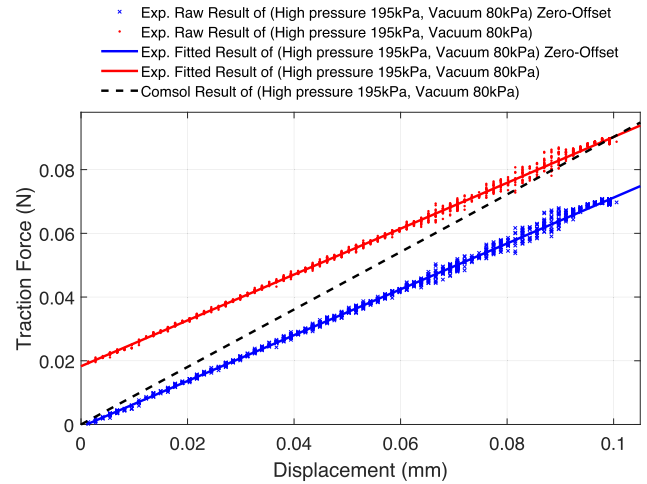
center, there is a nonuniformity of pressure in the vacuum chamber. Using this deeper vacuum source, the substrate touches the compliant surface close to the inlet port position, and not in the center, which shows that the vacuum suction force at the port area is stronger. Thus, the pressure in the vacuum chamber is nonuniform and depends on the location. As a result of this nonuniformity of the vacuum pressure in the vacuum chamber, the substrate flies at a nonuniform height above the system. This explains why there is a high traction force bias in Fig. 15, and why it is hard to deform the compliant surface with a certain movement to generate traction force linearly since one part of the substrate is probably already very close to the compliant surface.

To deal with this issue, the vacuum pump was moved much closer to the setup and most of the tubes were changed to bigger diameter ones to reduce the restriction in the path of the vacuum supply path and make the best use of the vacuum pump. Then, a new test based on the modified vacuum supply has been carried out. As shown in Fig. 18, the results show that: the maximum traction force is greatly increased to 90 mN; the relationship between displacement input and force output is more linear than the previous system; the force offset still exists but is twice smaller than before; there is still a clear deviation between the simulation result and experimental result; the saturation trend is almost eliminated. In a word, this modification of the vacuum supply system is effective.

D. Performance Discussion and Evaluation

Contactless force actuators have great potential for handling fragile substrates. Substrates can be transferred, actuated, and positioned in a mechanical contact-free manner to prevent breakages and contamination. In this work, a novel contactless force actuator integrated with a compliant active air-bearing surface has been designed and tested. A maximum actuation force of 90 mN is realized, which means more than 0.9 g acceleration can be reached for a normal 100 mm wafer with a thickness of 0.5 mm.

Even so, the deviation between the experimental results and the simulation results is still not negligible. This might be ascribed to the inherent offset of the system or the turbulent pressurized air after the inlet restrictors, or the coupling effect between the active air-bearing pressure and the wafer deformation (which could change the tilting status and the fly height). Notably, both the substrate alignment and the tilting are coupled with the pressure distribution, which can be addressed by scaling down the unit cell or reducing the net pressure difference.

Besides, several kinds of contactless systems for silicon substrates have been discussed, including electrostatic and air-based systems. Among them, electrostatic actuation systems can only output a force of less than 10 mN even when applying a high voltage to the subject [20]. As for the air-based systems, most of them can only perform the task of levitation for substrates, where the air jet is an exception. However, the air jet type can only provide a small actuation force (about 15 mN) at the cost of the introduction of turbulent air flows, which greatly hinders the application in the precision handling of fragile substrates [27]. Compared with the mentioned existing systems, our design based on active air-bearing has a much higher performance of the contactless actuation force and more stable laminar air flow underneath the substrate.

In addition to all the experimental data, a video is provided in the supplementary material, which shows a successful test where a hanging wire constrains the wafer from the top to make it stable. The result also shows that the developed system can effectively levitate and actuate the substrate in a linear mode on the x-axis and a rotational mode.

V. CONCLUSION

In this article, a contactless force actuator using an active air-bearing for handling substrates was designed, manufactured, and validated. This new design was developed based on a continuous deformable air-bearing surface composed of compliant-based actuation unit cells, which ensured the geometry of the active air-bearing to generate traction force effectively and improved the manufacturability greatly. Then the actuator overall was scaled down to have seven unit cells to actuate a 100 mm wafer without any mechanical contact. With the seven-unit-cell modular design, performance tests were carried out and evaluated. The results have shown that the proposed contactless actuator can levitate and actuate the substrate efficiently, where the maximum actuation force in the x-axis was determined to be 90 mN and a 42.5 μm fly height in the z-axis was achieved.

However, the developed system still needs to be further optimized considering its future applications, and specifically, the coupling effect between the active air-bearing pressure and the wafer deformation/alignment will be taken into account.

ACKNOWLEDGMENT

REFERENCES

[1] M. Neisser et al., "Lithography," in *Proc. IEEE Int. Roadmap Devices Syst. Outbriefs*, 2021, pp. 1–11.
[2] S. Spiller et al., "Processing of ultrathin 300 mm wafers with carrierless technology," in *Proc. IEEE 61st Electron. Compon. Technol. Conf.*, 2011, pp. 984–988.
[3] A. Dhadda, R. Montgomery, P. Jones, J. Heirene, R. Kuthakis, and F. Bieck, "Processing of ultrathin wafers for power chip applications," in *Proc. IEEE 14th Electron. Packag. Technol. Conf.*, 2012, pp. 649–653.
[4] Z. Dong and Y. Lin, "Ultra-thin wafer technology and applications: A review," *Mater. Sci. Semicond. Process.*, vol. 105, 2020, Art. no. 104681.
[5] Y.-J. Lee, B.-S. Kim, S. Ifitiquar, C. Park, and J. Yi, "Silicon solar cells: Past, present and the future," *J. Korean Phys. Soc.*, vol. 65, no. 3, pp. 355–361, 2014.
[6] R. Satpathy and V. Pamuru, "Chapter 4 - Making of crystalline silicon solar cells," in *Solar PV Power*. San Diego, CA, USA: Academic Press, 2021, pp. 71–134.
[7] M. R. Marks, Z. Hassan, and K. Y. Cheong, "Characterization methods for ultrathin wafer and die quality: A review," *IEEE Trans. Compon. Packag. Manuf. Technol.*, vol. 4, no. 12, pp. 2042–2057, Dec. 2014.
[8] H. Tang et al., "A monolithic force sensing integrated flexure bonder dedicated to flip-chip active soft-landing interconnection," *IEEE/ASME Trans. Mechatron.*, vol. 26, no. 1, pp. 323–334, Feb. 2021.
[9] J. Li, S. Zhang, J. Deng, and Y. Liu, "Development of a stepping piezo-electric actuator for an autofocus microscopic observation system," *IEEE Trans. Ind. Electron.*, vol. 71, no. 6, pp. 6107–6116, Jun. 2024.
[10] X. Yang, W.-L. Zhu, Z. Zhu, and L.-M. Zhu, "Design, assessment, and trajectory control of a novel decoupled robotic nanomanipulator," *IEEE/ASME Trans. Mechatron.*, vol. 27, no. 5, pp. 3999–4010, Oct. 2022.
[11] X. Wang, L. Zhu, and H. Huang, "A dynamic model of stick-slip piezo-electric actuators considering the deformation of overall system," *IEEE Trans. Ind. Electron.*, vol. 68, no. 11, pp. 11266–11275, Nov. 2021.
[12] Z. Guo, Z. Lyu, and Q. Xu, "Design of a piezoelectric-driven microgripper with three working modes," *IEEE/ASME Trans. Mechatron.*, vol. 29, no. 1, pp. 260–270, Feb. 2024.
[13] G. Zhao et al., "Nontraditional energy-assisted mechanical machining of difficult-to-cut materials and components in aerospace community: A comparative analysis," *Int. J. Extreme Manuf.*, vol. 6, no. 2, 2024, Art. no. 022007.
[14] J. Li, M. Sun, and Z. Chen, "An add-on damping enhancement with adjustable gain for lightly damped system," *Mech. Syst. Signal Process.*, vol. 191, 2023, Art. no. 110179.
[15] H. Zhu, T. J. Teo, and C. K. Pang, "Magnetically levitated parallel actuated dual-stage (Maglev-pad) system for six-axis precision positioning," *IEEE/ASME Trans. Mechatron.*, vol. 24, no. 4, pp. 1829–1838, Aug. 2019.
[16] W.-J. Kim and D. L. Trumper, "High-precision magnetic levitation stage for photolithography," *Precis. Eng.*, vol. 22, no. 2, pp. 66–77, 1998.
[17] "Multi-dimensional manufacturing with unprecedented flexibility," 2023. [Online]. Available:https://www.planarmotor.com/en
[18] W. B. Hoekwater, E. Ronaes, and H. HosseinNia, "Hybrid tunable magnet actuator: Design of a linearized force-flux tunable magnet actuator," *IEEE Trans. Ind. Electron.*, vol. 71, no. 5, pp. 5073–5082, May 2024.
[19] E. K. Kim, J. W. Jung, H. M. Yoon, and J. Y. Yoon, "Near-zero-power 2-DOF noncontact transportation by static and dynamic disturbance compensation using single-body PM-biased magnetic levitator," *IEEE/ASME Trans. Mechatron.*, vol. 29, no. 1, pp. 767–776, Feb. 2024.
[20] I. Morkvenaite-Vilkonciene, V. Bucinskas, J. Subaciute-Zemaitiene, E. Sutinys, D. Virzonis, and A. Dzedzickis, "Development of electrostatic microactuators: 5-year progress in modeling, design, and applications," *Micromachines*, vol. 13, no. 8, 2022, Art. no. 1256.
[21] J. Jin, T. C. Yih, T. Higuchi, and J. U. Jeon, "Direct electrostatic levitation and propulsion of silicon wafer," *IEEE Trans. Ind. Appl.*, vol. 34, no. 5, pp. 975–984, Sep./Oct. 1998.
[22] S.-K. Ro, S. Kim, Y. Kwak, and C. H. Park, "A linear air bearing stage with active magnetic preloads for ultraprecise straight motion," *Precis. Eng.*, vol. 34, no. 1, pp. 186–194, 2010.
[23] "Overview of end effectors," 2023. [Online]. Available: https://www.mechatronic.at/zh/our-technologies-alias/end-effectors-for-critical-wafers-alias

[24] "Contactless wafer handling and contactless handling in PV industry," 2023. [Online]. Available: https://www.zs-handling.com/en/contactless-wafer-handling

[25] M. Shi, S. Chen, H. Huang, L. Qin, and T. Liu, "Self-floating and self-rotating non-contact ultrasonic motor with single active vibrator," *Tribol. Int.*, vol. 180, 2023, Art. no. 108217.

[26] M. Li and X. Ma, "Study on the temperature in air squeeze film," in *Proc. Int. Conf. Mech. Des.*, 2021, pp. 49–63.

[27] B. Dahroug, G. J. Laurent, V. Guelpa, and N. Le Fort-Piat, "Design, modeling and control of a modular contactless wafer handling system," in *Proc. IEEE Int. Conf. Robot. Autom*, 2015, pp. 976–981.

[28] G. J. Laurent and H. Moon, "A survey of non-prehensile pneumatic manipulation surfaces: Principles, models and control," *Intell. Serv. Robot.*, vol. 8, no. 3, pp. 151–163, 2015.

[29] J. Wesselingh, "Contactless positioning using an active air film," Ph.D. dissertation, Dept. Precision Microsystems Eng., Delft Univ. Technol., Delft, Netherlands, 2011.

[30] P. H. Vuong, "Air-based contactless actuation system for thin substrates: The concept of using a controlled deformable surface," Ph.D. dissertation, Dept. Precision Microsystems Eng., Delft Univ. Technol., Delft, Netherlands, 2016.

[31] R. Hooijschuur, N. Saikumar, S. H. HosseinNia, and R. A. van Ostayen, "Air-based contactless wafer precision positioning system," *Appl. Sci.*, vol. 11, no. 16, 2021, Art. no. 7588.

[32] F. Al-Bender, *Air Bearings: Theory, Design and Applications.* Hoboken, NJ, USA: Wiley, 2021.

[33] "Thin-film flow," 2023. [Online]. Available: https://doc.comsol.com/5.5/doc/com.comsol.help.mems/mems_ug_fluidflow.07.16.html

[34] S. Srivastava, R. K. Garg, V. S. Sharma, and A. Sachdeva, "Measurement and mitigation of residual stress in wire-arc additive manufacturing: A review of macro-scale continuum modelling approach," *Arch. Comput. Methods Eng.*, vol. 28, pp. 3491–3515, 2021.

Ron A. J. van Ostayen received the Ph.D. degree in mechanical enigneering from Delft University of Technology, Delft, The Netherlands, in 2002.

He is currently an Associate Professor of mechatronic system design and tribotronics with the Department of Precision and Microsystems Engineering, Delft University of Technology, Delft, The Netherlands. He has authored or coauthored in national and international journals, at numerous conferences and workshops, and holds patents mainly in the field of full film tribology. His stay at Delft has been interspaced with inspirational sabbatical leaves at MIT, Cambridge (USA) and TUM, Munchen (Germany). The study and development of active tribological machine components, e.g., bearings with integrated sensing or surface shape actuation, is part of an emerging new technology field referred to as tribotronics. His research interests include tribology, the study of friction, wear, and lubrication in mechanical and mechatronical systems, with a long-standing interest in the study of the fundamental properties of full film lubrication through mathematical modeling and experimental study.

Sifeng He received the B.Sc. and M.S. degrees in mechanical engineering from the School of Electromechanical Engineering, Guangdong University of Technology, Guangzhou, China, in 2018 and 2021, respectively. He is currently working toward the Ph.D. degree in mechanical engineering with the Department of Precision and Microsystems Engineering, Delft University of Technology, Delft, The Netherlands.

His research interests include wafer handling systems, contactless actuation, compliant mechanisms, nanopositioning systems, and mechatronics applications in semiconductor industries.

S. Hassan HosseinNia (Senior Member, IEEE) received the Ph.D. degree (Hons.) (*cum laude*) in electrical engineering specializing in automatic control: application in mechatronics from the University of Extremadura, Badajoz, Spain, in 2013.

He has an industrial background, having worked with ABB, Sweden. Since October 2014, he has been appointed as a Faculty Member with the Department of Precision and Microsystems Engineering, Delft University of Technology, Delft, The Netherlands. He has coauthored over 150 publications in respected journals, conference proceedings, and book chapters. His main research interests include precision mechatronic system design, precision motion control, and mechatronic systems with distributed actuation and sensing.

Dr. HosseinNia served as the General Chair of the 7th IEEE International Conference on Control, Mechatronics, and Automation (ICCMA 2019). Currently, he is an editorial board member of "*Fractional Calculus and Applied Analysis*," "*Frontiers in Control Engineering*," and "*International Journal of Advanced Robotic Systems (SAGE)*."